Dispersion curve regression - assisted wideband local wavenumber analysis for characterizing three-dimensional (3D) profile of hidden corrosion damage

Zhenhua Tian[1*], Wenfeng Xiao[2], Zhaoyun Ma[2], Lingyu Yu[2*]

[1] *Department of Aerospace Engineering, Mississippi State University, Starkville, MS, 39759*

[2] *Department of Mechanical Engineering, University of South Carolina, Columbia, SC, 29208*

[*] *Corresponding author: Z.T. (tian@ae.msstate.edu) and L.Y. (yu3@cec.sc.edu)*

Abstract:

Corrosion as common damage in civil, petrochemical, nuclear, and aerospace structures affects the integrity and safety of the structures and may lead to catastrophic failures. This paper presents dispersion curve regression-assisted local wavenumber analysis method, which can analyze the time-space wavefield containing wideband information of wave-damage interaction and further extract the structural information carried by such wavefield for characterizing hidden corrosion damage in an isotropic plate. To acquire the time-space wavefield, a noncontact scanning laser Doppler vibrometer is used. In our analysis method, the acquired time-space wavefield is firstly processed to generate a local wavenumber function. The derived wavenumber function is further analyzed with a dispersion curve regression step, which searches in a set of theoretical frequency-wavenumber dispersion curves for different plate thicknesses and identifies the optimal plate thickness whose theoretical curve best matches the frequency-wavenumber relation contained in the local wavenumber function. By this means, a 3D profile including both in plane and thickness dimensions of the structure can be constructed for corrosion visualization and quantification. The experimental study demonstrates that our method can quantify the profile of hidden uniform corrosion in metal plates in terms of its in-plane shape and size as well as its out-of-plane depth in the subwavelength scale. Moreover, compared to previous Lamb wave-based corrosion inspection methods, our technique allows for noncontact 3D characterization of hidden corrosion from a far distance to the structure. We believe this work will inspire new 3D

damage quantification methods that are based on wavefield analysis as well as enable potential applications for the quantification of hidden corrosion in civil, petrochemical, nuclear, and aerospace structures.

Keywords: Lamb waves, Laser Doppler vibrometry, wavefield analysis, local wavenumber analysis, corrosion inspection

1. Introduction

Corrosion, the deterioration of a substance (usually a metal) or its properties because of a reaction with its environment [1], is common damage in civil, petrochemical, nuclear, aerospace, and many other engineering structures. According to the technical report of the National Association of Corrosion Engineers (NACE) released in 2016, the global cost of corrosion is estimated to be US$2.5 trillion [2]. Among various types of corrosion, the uniform corrosion is a typical cumulative wall thickness reduction damage, while the pitting corrosion is a typical localized corrosion attack in which small volumes of material are removed to produce craters or pits that may culminate in complete perforation of the structure [3]. When the corrosion surface is hidden from the sight such as internal corrosion of pressure vessels and corrosion of buried or immersed structures, the corrosion is difficult to be evaluated through visual inspection and often referred to as hidden corrosion. Moreover, the hidden corrosion that gradually cumulates during a long-term service may impair the structural integrity, shorten the structural lifetime, affect the safety and reliability of the system, and lead to catastrophic failures. The visualization and quantification of hidden corrosion through advanced nondestructive evaluation (NDE) are essential for detecting the corrosion location, quantifying the corrosion size and depth, ensuring the safety of structures, and reducing the life-cycle cost.

Among various NDE methods, Lamb wave based methods have proven to be an effective and efficient method for the rapid inspection of large plate-like structures, because Lamb waves have the high sensitivity to various types of small defects as well as the capability of traveling relatively long distances with low energy loss [4-6]. With these features, Lamb wave-based methods have been developed to detect and visualize corrosion in metal plates by using sensor arrays or networks [7-12]. Chen et al. employed sparse arrays of piezoelectric transducers (PZTs) for detecting a quasi-circular uniform chemical corrosion using probability-based diagnostic imaging method in submerged plates [7]. Gorgin et al. developed a damage size characterization method using pure fundamental antisymmetric A_0 Lamb wave mode using PZT network and showed how it was used to estimate the thickness of simulated uniform corrosion [8]. Recently, Rao et al. developed a Lamb wave tomography method using a circular PZT array and A_0 mode to generate thickness maps during the process of forced electrochemical corrosion [9]. In addition, corrosion depth quantification based on the dispersion feature of Lamb waves (the group/phase velocity depends on the frequency-thickness product) has also been explored [13-18]. Yu et al. and Nagy et al. found that the phase velocity of the low-frequency A_0 mode gradually decreases with the increase of the corrosion depth [13, 14]. As a result, the acquired signal of the low-frequency A_0 mode exhibits a phase lag when corrosion presents. Huthwaite et al. found that the sensitivity of Lamb waves to the thickness variation depends on the gradient of the dispersion curve [15]. A steep gradient could result in a large velocity change, and hence a high sensitivity to the thickness variation. Based on the velocity change induced by the thickness variation, Jenot et al. proposed a corrosion thickness gauging method for metal plates [16]. Despite the advancements in corrosion detection and depth quantification, it is still challenging to use Lamb wave-based methods to detect the location, visualize the shape, quantify the size, and determine the depth profile of corrosion damage. Additionally, few Lamb wave-based

methods can quantify the corrosion depth with the resolution and accuracy in the deep subwavelength scale (i.e. the damage dimension is smaller than one tenth of the inspection wavelength).

As seen in most previous studies for corrosion inspection, PZT sensors are often used and installed on plates in simple pitch-catch/pulse-echo layouts, or as complicated networks. Once PZTs are installed, it becomes cumbersome to reconfigure the sensor arrangement for different scenarios. Moreover, the spatial sensing resolution is limited by the dimension of the sensor itself. Recently, the scanning laser Doppler vibrometer (SLDV) attracts great interests for Lamb wave-based damage detection, visualization, and quantification [19-26]. Based on the Doppler effect, the SLDV can acquire velocities/displacements of Lamb waves at the laser inspection spot. By scanning high-density points in the desired area, the SLDV can acquire a high-resolution (less than 1 mm) velocity/displacement wavefield, which contains a wealth of time-space information about the Lamb wave propagation and wave interaction with damage. Compared to PZT sensors, SLDV offers several advantages, such as noncontact Lamb wave acquisition from a far distance to the structure, high flexibility of moving the laser spot for reconfigurable sensing, in addition to the high spatial sensing resolution. More importantly, the acquired multidimensional time-space wavefields by the SLDV enables the processing of Lamb wave signals in the wavenumber domain [22, 27, 28]. SLDV based Lamb waves have been used for visualization and detailed quantification of various types of defects, such as cracks, delamination, and debonding [28-31]. However, it is still less studied how to construct the structural 3D profile (in-plane and thickness) with only 2D measurement (in-plane scanning) using conventional wavefield analysis methods. Moreover, most existing wavefield analysis methods use wavefield data in a narrow frequency band with limited frequency-wavenumber

information. Furthermore, limited studies have reported successful quantification of corrosion depths that are in the subwavelength scale.

This paper presents a new wavefield analysis method, namely, dispersion curve regression assisted wideband local wavenumber analysis, which is able to derive the structural information from wideband time-space wavefields and construct 3D profiles of plates with corrosion damage. Our method has been experimentally validated on plates containing uniform corrosion defects (typical cumulative wall thickness reduction defects) with different depths. The experimental validation demonstrates that the results of the imaging method not only provides in-plane corrosion profile including its shape and size but also gives its depth of subwavelength scale. The remainder of this paper is organized as follows: Section 2 presents the dispersion curve regression-assisted wideband local wavenumber analysis method; Section 3 and 4 present the experimental studies for the demonstration and validation of the usage of our method for corrosion 3D profile quantification; Section 5 concludes the paper with findings, discussions, and future work.

2. Dispersion curve regression-assisted wideband local wavenumber analysis

This section presents our wavefield analysis method, the dispersion curve regression-assisted wideband local wavenumber analysis. Figure 1 is an overview of the analysis method. A PZT-SLDV sensing system is used for the time-space wavefield (e.g., Figure 1b) acquisition in our study. The acquired time-space wavefield will be transformed to a space-frequency wavefield (e.g., Figure 1c) and then processed by the local wavenumber analysis, resulting in a local wavenumber function (e.g., Figure 1d), which contains the information of the frequency-wavenumber relation at each sensing position. This experimentally acquired frequency-wavenumber information will be used in the subsequent dispersion regression step to search

within a set of theoretical frequency-wavenumber dispersion and to determine the thickness of a point at which the experimental and theoretical dispersion relations have the best matches. By repeating the regression step for all the scanning points, a thickness map (e.g. Figure 1e) that can show both the location and dimension (i.e. profile) of the corrosion and its thickness is generated. Details of the local wavenumber analysis and the dispersion curve regression are given in the following two subsections.

2.1. Wideband local wavenumber analysis

For the completeness of presenting the wideband local wavenumber analysis method, the sensing system used for time-space wavefield acquisition is briefly explained here. More details of experimental setup for corrosion characterization are to be given in Section 3. As illustrated in the schematic in Figure 1a, a PZT wafer is bonded on the top surface of the plate to generate Lamb waves, while a noncontact SLDV (model: Polytec PSV-400-M2) is used to acquire out-of-plane velocities/displacements of Lamb waves based on the Doppler effect by setting the laser beam normal to the test plate. More information about the PZT-SLDV sensing system can be found in our previous work [23]. Through point-by-point measurement at multiple scan points in a user-defined grid, the SLDV acquires Lamb waves wavefield $v(t, \mathbf{x})$ as a function of both time t and location $\mathbf{x}$. Compared to acquiring Lamb wave signals with a small number of loosely distributed sensors used in other Lamb wave-based techniques [32-35], the acquisition of a time-space wavefield $v(t, \mathbf{x})$ from densely distributed points allows one to obtain the wavenumber information of wave propagation. To properly acquire the wavenumber information of Lamb waves, Shannon sampling theorem in space shall be observed that the spatial resolution of the wavefield acquisition should be smaller than a half of the minimum wavelength being used. The same applies to sampling in time that the sampling frequency should be at least twice of the maximum wave frequency being used.

The acquired time-space wavefield $v(t, \mathbf{x})$ (Figure 1b) is first transformed to a frequency-space wavefield $V(f, \mathbf{x})$ through Fourier transform, followed with the short-space Fourier transform given in [36] to derive a space-frequency-wavenumber representation $S(\bar{\mathbf{x}}, f, \mathbf{k})$, as:

$$S(\bar{\mathbf{x}}, f, \mathbf{k}) = \int_{-\infty}^{\infty} \int_{-\infty}^{\infty} V(f, \mathbf{x}) W(\mathbf{x} - \bar{\mathbf{x}}) e^{j\mathbf{k} \cdot \mathbf{x}} d\mathbf{x} \tag{1}$$

where $\bar{\mathbf{x}}$ is the retained spatial vector $(\bar{x}, \bar{y})$, and $W(\mathbf{x})$ is a spatial window function. In this study, a Hanning function is used to construct the window $W(\mathbf{x})$, given as:

$$W(\mathbf{x}) = \begin{cases} \dfrac{1}{2}\left[1 + \cos\left(2\pi \dfrac{|\mathbf{x}|}{D_x}\right)\right] & \text{if } |\mathbf{x}| \leq D_{\mathbf{x}}/2 \\ 0 & \text{otherwise} \end{cases} \tag{2}$$

where D_x is the window length in the space. The obtained space-frequency-wavenumber representation $S(\bar{\mathbf{x}}, f, \mathbf{k})$ can indicate how the wave strength varies with respect to space $\bar{\mathbf{x}}$, frequency f, and wavenumber $\mathbf{k}$. The window size D_x determines the spatial and wavenumber resolutions of the short-space Fourier transform. With the increase of window size D_x, the wavenumber resolution increases, while the spatial resolution of the short-space Fourier transform decreases. Therefore, depending on the usage of the short-space Fourier transform, one can optimize the window size. In this research, the window size D_x used for all the analyses equals two wavelengths. More details can be found in in [36].

Given the space-frequency-wavenumber representation $S(\bar{\mathbf{x}}, f, \mathbf{k})$, a local wavenumber function $k_{sw}(\bar{\mathbf{x}}, f)$ can be defined by finding the wavenumber where $S(\bar{\mathbf{x}}, f, \mathbf{k})$ achieves its maximum amplitude at a given location $\bar{\mathbf{x}}$ and frequency f, as:

$$k_{sw}(\bar{\mathbf{x}}, f) = \left| \mathbf{k}_{sw}(\bar{\mathbf{x}}, f) \right| \tag{3}$$

with,

$$\mathbf{k}_{sw}(\bar{\mathbf{x}}, f) = \arg\max_{\mathbf{k}} \left| S(\bar{\mathbf{x}}, f, \mathbf{k}) \right| \tag{4}$$

The Eq.(4) identifies the wavenumber $\mathbf{k}_{sw}(\overline{\mathbf{x}}, f)$ by identifying the wavenumbers which are associated with the highest amplitude in the spectrum function $|S(\overline{\mathbf{x}}, f, \mathbf{k})|$ at position $\overline{\mathbf{x}}$ and frequency f. The process is regardless of the wave modes and only depends on the values of the wave amplitudes. The resulted function $k_{sw}(\overline{\mathbf{x}}, f)$ can be interpreted as a distribution of wavenumbers in the space defined by $\overline{\mathbf{x}}$ at the frequency f.

For Lamb waves, at a given frequency f_i, the wavenumber changes with respect to the plate thickness. Based on this principle, the local wavenumber function $k_{sw}(\overline{\mathbf{x}}, f_i)$, which captures the wavenumber variation in the 2D space (i.e. x and y dimensions) can be used for 2D visualization of the corrosion shape and quantification of the corrosion location and size. However, the local wavenumber function with the information at a single frequency could be subjected to high noises and low fidelity. This limitation will be further discussed with the experimental data in Section 3. To address this limitation, we propose to fuse the wavenumber information within a wide frequency band and average the set of $k_{sw}(\overline{\mathbf{x}}, f_i)$ obtained at each frequencies f_i, as:

$$k_{sw}(\overline{\mathbf{x}}) = \frac{1}{N} \sum_{i=1}^{N} k_{sw}(\overline{\mathbf{x}}, f_i),$$ (5)

Where the resulting $k_{sw}(\overline{\mathbf{x}})$ is the derived averaged local wavenumber function and f_i ($i = 1, 2, 3\dots N$) represents the selected frequencies from a wide frequency band.

2.2. Dispersion curve regression for thickness characterization

For Lamb waves in plates, the frequency-wavenumber dispersion relations change with respect to the plate thickness, as illustrated in Figure 2. Hence, the remaining plate thickness, as well as the corrosion depth, can be determined by using the frequency-wavenumber relation in the local wavenumber function $k_{sw}(\overline{\mathbf{x}}, f)$. In this work, a novel dispersion curve regression method is developed to derive the thickness information from the local wavenumber function $k_{sw}(\overline{\mathbf{x}}, f)$ so

that we can achieve 3D visualization and quantification of corrosion that includes not only the in-plane dimension but also the thickness values.

A least square regression is used to search in a collection of theoretical frequency-wavenumber dispersion curves for different plate thicknesses and identify the plate thickness, whose theoretical curve best fits the frequency-wavenumber relation contained the local wavenumber function $k_{sw}(\overline{\mathbf{x}}, f)$. By doing the regression for all the coordinates $\overline{\mathbf{x}}$, a map of the thickness of the plate $d(\overline{\mathbf{x}})$ can be constructed, as:

$$d(\overline{\mathbf{x}}) = \arg \min_d \sum_{i=1}^{N} \left[k_{sw}(\overline{\mathbf{x}}, f_i) - k(f_i, d) \right]^2 \tag{6}$$

where f_i (i = 1, 2, 3… N) represents a series of selected frequencies over the frequency band of interest and $k(f_i, d)$ represents the theoretical wavenumber with respect to frequency and thickness. The resulted thickness map $d(\overline{\mathbf{x}})$ contains the thickness information at the location $\overline{\mathbf{x}}$, and therefore indicates the presence and extent of the corrosion, giving its location, depth, and approximate size.

The thickness quantification sensitivity is related to the wavenumber change induced by plate thickness change, as shown in Figure 2. Within a given frequency range, if the dispersion curve has higher nonlinearity, the wavenumber will change more significantly for plates with different thicknesses. And therefore, the sensitivity of the plate thickness quantification method becomes higher. As manifested in Figure 2, we see that within the frequency range 0~600 kHz the A0 mode's dispersion curve has higher nonlinearity than that of the S0 mode; therefore A0 mode's wavenumber is more sensitive to the plate thickness change. On the other hand, the S0 mode is correspondingly more sensitive to the plate thickness change in the frequency range 600~800 kHz

3. Experimental validation through the imaging of hidden uniform corrosion

Uniform corrosion is a common form of corrosion attack with an even, regular loss of metal from the corroding surface [3]. When the corroding surface is hidden from sight, such as internal corrosion of pressure vessels and corrosion of buried or immersed structures, the corrosion attack is difficult to be detected. In this Section, experiments are performed to validate the developed the dispersion curve regression-assisted local wavenumber analysis method and demonstrate the capability of our method for characterizing the 3D profiles of uniform corrosion defects with different depths in the range from 0.25 to 1 mm.

3.1. Experiments on a plate with hidden uniform corrosion

The test specimen is an aluminum 6061-T6 plate ($610 \times 610 \times 3.2$ mm^3) with uniform corrosion simulated by a circular flat-bottom hole of 25.4 mm diameter in the back surface of the plate. The uniform corrosion is created through milling. The corrosion depth is gradually extended to four different values of 0.25, 0.50, 0.75 and 1.00 mm. A photo of the uniform corrosion with a depth of 0.50 mm is illustrated in the inset of Figure 3a.

A photo of the experimental setup and a schematic of the sensing layout with dimensions are given in Figure 3a and b, respectively. A round PZT actuator (APC 851 by American Piezo, diameter of 7 mm, thickness of 0.2 mm) is bonded on the front surface of the plate to excite Lamb waves. The center of the PZT is set as the Cartesian coordinate origin O for subsequent wave propagation study, and the center of the uniform corrosion is at (0, 60) mm. An arbitrary waveform function generator (Hewlett Packard 33120A) is used to generate the excitation signal, which is amplified to 40 Vpp by a voltage amplifier (Krohn-Hite 1506). An SLDV (model: Polytec PSV-400-M2) is used to measure the out-of-plane displacement components of Lamb waves and acquire the time-space wavefield in a predefined rectangular scanning area (80×80

mm^2) with a spatial scanning resolution of 0.4 mm from the front surface of the plate. The time sampling rate is 5.12 MHz.

In this experiment, a wideband chirp signal (Figure 3c) with a duration of 50 μs is used for Lamb wave excitation. The frequency spectrum (Figure 3d) of the chirp signal shows relatively high and stable amplitudes in the frequency range of 300 – 800 kHz. Compared to narrowband tone burst signals, the wideband chirp signal covers wider frequencies range, and hence is more suitable for the dispersion curve regression by providing enhanced accuracy and high robustness to the analysis presented in Section 2. Additionally, the acquired wideband wavefields will contain more information of the wave-damage interaction.

3.2. Results of corrosion imaging and wall thickness quantification

Through laser Doppler vibrometry, a time-space wavefield of Lamb waves generated by the PZT actuator with the wideband chip excitation is acquired. Figure 4a to d plot the acquired wavefields at 30, 40, 50, and 60 μs on the plate with 0.75 mm corrosion depth. It can be seen that as time increases the wavelengths in the acquired wavefields gradually become smaller. This observation is reasonable since as the frequency increases with time in the chirp signal; the wavelength will decrease accordingly due to their inverse relation. In addition, the acquired wavefield at 30 μs shows two Lamb wave modes, a stronger A_0 mode and a weaker S_0 mode. This is due to the fact that the SLDV is set to measure only the out-of-plane motions of Lamb waves [36] while the A_0 mode has stronger out-of-plane motions than the S_0 mode within this frequency range. Because the A_0 mode has higher amplitudes, the derived local wavenumber function based on Eq. (4) should mainly contain the information of the A_0 mode.

By applying Fourier transform to the acquired time-space wavefield $v(t, \mathbf{x})$, a frequency-space wavefield $V(f, \mathbf{x})$ is obtained. Figure 5a to c plot the obtained wavefield samples at frequencies of 300, 500, and 800 kHz, respectively, when the corrosion depth is 0.75 mm. The

wavefield samples at different frequencies show different wave-corrosion interaction patterns, which are due to the combined effects of wave reflection, scattering, interference, and diffraction. Although the interaction patterns can indicate the existence of a structural discontinuity, without further postprocessing the patterns are difficult to directly provide quantitative information such as the location, size, and depth of corrosion damage.

To further characterize the corrosion, local wavenumber analysis is applied to the wavefields shown in Figure 5a to c. The constructed local wavenumber distributions at frequencies of 300, 500, and 800 kHz are given in Figure 5d to f. These distributions have highlighted areas with large wavenumbers due to the very small thickness at the corrosion site, and these areas indeed coincide with the actual corrosion (indicated by a solid circle). However, the single-frequency local wavenumber distributions in Figure 5d to f exhibit high noises. The wavenumber averaging process given by Eq. (5) is subsequently applied within the frequency band 300 – 800 kHz and the resulted averaged wavenumber distribution is presented in Figure 5g as an intensity image. The high intensity points in the plate correspond to large wavenumbers caused by the thickness reduction at the corrosion. Compared to single-frequency local wavenumber distributions in Figure 5d to f, the averaged result in Figure 5g shows lower noises and more discernible profile of the corrosion area, more agreeing with the actual circular shape corrosion.

Although the averaged local wavenumber distribution in Figure 5g has quantified the corrosion location, in-plane size, and shape, the corrosion depth is not determined. To construct the 3D (both in-plane and thickness) profile of the corrosion damage, the dispersion curve regression method developed in Section 2 is now adopted to the local wavenumber function. Figure 6 gives an example of the dispersion curve regression at the location of (0, 60) mm, where the actual plate thickness is 2.45 mm (i.e., the corrosion depth is 0.75 mm). The experimental data (triangles) are extracted from the local wavenumber function $k_{sw}(\bar{\mathbf{x}}, f)$. Through the

dispersion curve regression, the dispersion curve (solid line) that best matches the experimental data is found. The dotted and broken lines in Figure 6 represent the upper and lower boundaries for the 95% confident region. Using regression given in Eq. (6), the wall thickness at the location of (0, 60) mm can be found about 0.78 mm with the standard derivation of 0.12 mm. By applying the dispersion curve regression to all the points in the entire inspection area, a thickness map can be constructed for characterizing the 3D profile of corrosion damage.

The constructed thickness maps for the tested aluminum plate are given in Figure 7a, c, e, and g, when the corrosion defects have depths of 0.25, 0.50, 0.75, and 1.00 mm, respectively. The thickness maps show detected corrosion defects as high-intensity areas (small thickness regions), which agree very well with the actual corrosion areas (indicated by solid circles). These small thickness regions not only indicate the locations but also show the sizes and shapes of corrosion defects with different depths. Moreover, the thickness maps can indicate the remaining plate thickness distributions and be further used to quantitatively evaluate the corrosion depths (or thickness reductions).

To better illustrate the thickness quantification capability of our method, thickness profiles along a line $y = 60$ mm across the corrosion center are extracted, as shown in Figure 7b, d, f and h for the four cases with various depths. It can be seen that the thickness profiles (broken lines) extracted from the constructed thickness maps agree well with the actual thickness profiles (solid lines) in most regions, except the regions near the corrosion edges where the actual thickness profile has sudden changes. Notably, the minimum corrosion depth being examined in our work is only 0.25 mm while the wavelengths of the waves being used for inspection are in the range of 3.4 to 7.7 mm within the 300 to 800 kHz frequency band. Also, in most positions except those near the corrosion edges, the thickness quantification errors are less than 80 μm, which is

significantly smaller than the wavelengths. Our experimental results therefore manifest that our analysis method is able to quantify subwavelength-scale damage depths with microscale errors.

4. Imaging of pitting corrosion

As a common type of localized corrosion attack, the pitting corrosion usually has very small volumes of material removed from random areas on the surface, resulting in small craters or pits that may culminate in complete perforation of the structure [3]. Compared to uniform corrosion, pitting corrosion is more difficult to detect, especially at its early stage. In this section, experiments are attempted on this more complex type of corrosion for characterizing a cluster of simulated pitting corrosion in the hidden side of an aluminum plate.

4.1. Experiments on a plate with hidden pitting corrosion

Figure 8a plots a schematic of the experimental setup. The test specimen is an aluminum 6061-T6 plate ($610 \times 610 \times 3.2$ mm^3) with pitting corrosion in the back surface of the plate, simulated by a cluster of 3×3 pits with the center of the cluster at $(0, 60)$ mm (Figure 8b). The pits are hemispherical with a diameter of 2 mm, and the gaps between adjacent pits are 2 mm in both x and y directions. The sensing setup for the laser vibrometry test remains the same as that used in Section 3.

4.2. Results generated through local wavenumber analysis

The Lamb waves generated by the PZT with the chirp excitation in the frequency band of 300 – 800 kHz are acquired by SLDV. Through the wavefield filtering [36], a pure A_0 mode is extracted from the acquired wavefield. For illustration purposes, Figure 9a plots the filtered A_0 wavefield at 500 kHz. Although strong incident waves are seen propagating to the pitting corrosion area (indicated by a cluster of 3×3 circles), barely any waves scattering or

interrupting can be observed. This means the effects of small shallow pits on the incident Lamb waves are too weak to be immediately observed from the original wavefield.

Using the wavenumber analysis and dispersion curve regression presented in Section 2, the averaged local wavenumber distribution (Figure 9b) is obtained by using the wavenumber information in the frequency range of 300 – 800 kHz. The thickness map derived by dispersion curve regression is given in Figure 9c. Both imaging results show high-intensity areas around the location of (0, 60) mm. These identified areas agree with the actual region with the corrosion cluster. Both imaging results successfully identify the region with a pit cluster and roughly quantify the size of the pitting area. However, the resolutions of both imaging results are not fine enough to resolve individual pits or quantify the number of pits. A possible reason is that the wavenumber changes induced by the subwavelength shallow pits are extremely small. Compared to the wavelength of the A_0 mode at 500 kHz (5.2 mm), the size of the pits (with the depth and radius of 1 mm) and the spacing between adjacent pits (2 mm) are smaller than a half of the wavelength.

5. Conclusions and Discussions

This paper presents a dispersion curve regression-assisted wideband local wavenumber analysis method which can process the time-space Lamb waves wavefield of a wide frequency band and generate a 3D profile of the corrosion damage in terms its in-plane sizes, shape, location, as well as depth. The in-plane evaluation is achieved through the adoption of wideband Lamb wave propagation as well as an imaging algorithm with enhanced fidelity, improved resolution, and reduced background noise, compared to the results generated with conventionally used single frequency method. On the other hand, the subwavelength thickness evaluation is achieved

through the dispersion curve regression-assisted analysis and thickness maps of the plates are constructed to give immediate indications of the thickness change caused by corrosion.

Experiments have been performed to demonstrate the 3D evaluation of circular-shaped uniform corrosion with different depths including 0.25, 0.5, 0.75, and 1 mm in aluminum plates containing. We showed that the corrosion locations, sizes, and shapes given through the derived thickness maps agree well with those of the actual corrosion defects. The thickness profiles obtained from the thickness maps, on the other hand, also agree well with the actual thickness at most positions of the corrosion, except those near the corrosion edges where the actual thickness profiles have sudden changes due to machining. The minimum corrosion depth being detected in our study is as small as 0.25 mm, much smaller than the wavelengths being used for inspection, showing that the present method is able to quantify damage of subwavelength scale.

Compared to conventional wavefield analysis methods, our analysis method uniquely (1) makes use of wideband Lamb waves to enhance overall imaging quality and (2) gives 3D (i.e. in-plane and thickness) evaluation of representative corrosion damage in plate-like structures through the dispersion curve regression in the local wavenumber analysis. The detection results are quite promising, showing that uniform corrosion of subwavelength scale can be detected and quantified with high accuracy. It offers itself as an unprecedented method to localize the corrosion damage, visualize its shape, quantify its size, and determine the subwavelength depth.

Despite of the advantages listed above, there are some limitations that need to be addressed in the future. There in-plane imaging resolution for pitting corrosion with subwavelength in-plane dimension still needs to be improved. The present method was not able to identify the individual tiny pits (with both subwavelength-scale sizes and depths) in a cluster. Possible reasons are that the wavenumber change induced by small shallow pits is subtle, and the in-plane distance between adjacent pits is less than a half wavelength. In addition, the current imaging

method mainly relies on the damage information carried by local waves presented in the damage region. The damage information carried by waves that propagate away from the damage region is not effectively used in the imaging method presented in this study. In fact, these waves could carry a wealth of information that can be used for damage imaging. Further development will be made in this regard. Last but not least, numerical simulations and more experiments shall be explored to support the understanding and further development of our wavefield analysis method.

6. Acknowledgments

7. References

[1]   G. H. Koch, M. P. H. Brongers, N. G. Thompson, Y. P. Virmani, and P. J. H., *Corrosion costs and preventive strategies in the united states*. Houston, TX: National Association of Corrosion Engineers (NACE) International, 2001.

[2]   G. Koch, J. Varney, N. Thompson, O. Moghissi, M. Gould, and J. Payer, *International measures of prevention, application, and economics of corrosion technologies study*. Houston, TX: National Association of Corrosion Engineers (NACE) International, 2016.

[3]   P. R. Roberge, *Corrosion engineering principles and practice*. New York, NY: McGraw-Hill Companies, Inc, 2008.

[4]   J. L. Rose, *Ultrasonic waves in solid media*. Cambridge, UK: Cambridge University Press, 1999.

[5]   W. J. Staszewski, C. Boller, and G. R. Tomlinson, *Health monitoring of aerospace structures*. Chichester, UK: John Wiley & Sons, 2004.

[6]   V. Giurgiutiu, *Structural health monitoring with piezoelectric wafer active sensors*. Boston, MA: Academic Press, 2008.

[7]   J. G. Chen, Z. Q. Su, and L. Cheng, "Identification of corrosion damage in submerged structures using fundamental anti-symmetric lamb waves," *Smart Materials and Structures,* 19 (1), p. 015004, 2010.

[8]   R. Gorgin, Z. J. Wu, D. Y. Gao, and Y. S. Wang, "Damage size characterization algorithm for active structural health monitoring using the a(0) mode of lamb waves," *Smart Materials and Structures,* 23 (3), p. 035015, 2014.

[9]   J. Rao, M. Ratassepp, D. Lisevych, M. H. Caffoor, and Z. Fan, "On-line corrosion monitoring of plate structures based on guided wave tomography using piezoelectric sensors," *Sensors,* 17 (12), p. 2882, 2017.

[10] V. T. Rathod and D. R. Mahapatra, "Ultrasonic lamb wave based monitoring of corrosion type of damage in plate using a circular array of piezoelectric transducers," *Ndt & E International,* 44 (7), pp. 628-636, 2011.

[11] D. J. Wang, W. F. Zhang, X. Y. Wang, and B. Sun, "Lamb-wave-based tomographic imaging techniques for hole-edge corrosion monitoring in plate structures," *Materials,* 9 (11), p. 916, 2016.

[12] R. Sicard, A. Chahbaz, and J. Goyette, "Guided lamb waves and l-saft processing technique for enhanced detection and imaging of corrosion defects in plates with small depth-to-wavelength ratio," *Ieee Transactions on Ultrasonics Ferroelectrics and Frequency Control,* 51 (10), pp. 1287-1297, 2004.

[13] L. Yu, V. Giurgiutiu, J. Wang, and Y. J. Shin, "Corrosion detection with piezoelectric wafer active sensors using pitch-catch waves and cross-time–frequency analysis," *Structural Health Monitoring,* 11 pp. 83-93, 2012.

[14] P. B. Nagy, F. Simonetti, and G. Instanes, "Corrosion and erosion monitoring in plates and pipes using constant group velocity lamb wave inspection," *Ultrasonics,* 54 (7), pp. 1832-1841, 2014.

[15] P. Huthwaite, R. Ribichini, P. Cawley, and M. J. S. Lowe, "Mode selection for corrosion detection in pipes and vessels via guided wave tomography," *Ieee Transactions on Ultrasonics Ferroelectrics and Frequency Control,* 60 (6), pp. 1165-1177, 2013.

[16] F. Jenot, M. Ouaftouh, M. Duquennoy, and M. Ourak, "Corrosion thickness gauging in plates using lamb wave group velocity measurements," *Measurement Science and Technology,* 12 (8), pp. 1287-1293, 2001.

[17] J. Bingham and M. Hinders, "Lamb wave characterization of corrosion-thinning in aircraft stringers: Experiment and three-dimensional simulation," *Journal of the Acoustical Society of America,* 126 (1), pp. 103-113, 2009.

[18] J. Pei, M. I. Yousuf, F. L. Degertekin, B. V. Honein, and B. T. KhuriYakub, "Lamb wave tomography and its application in pipe erosion/corrosion monitoring," *Research in Nondestructive Evaluation,* 8 (4), pp. 189-197, 1996.

[19] W. J. Staszewski, B. C. Lee, and R. Traynor, "Fatigue crack detection in metallic structures with lamb waves and 3d laser vibrometry," *Measurement Science & Technology,* 18 (3), pp. 727-739, 2007.

[20] H. Sohn, D. Dutta, J. Y. Yang, M. DeSimio, S. Olson, and E. Swenson, "Automated detection of delamination and disbond from wavefield images obtained using a scanning laser vibrometer," *Smart Materials & Structures,* 20 p. 045017, 2011.

[21] T. E. Michaels, J. E. Michaels, and M. Ruzzene, "Frequency-wavenumber domain analysis of guided wavefields," *Ultrasonics,* 51 pp. 452-466, 2011.

[22] M. D. Rogge and C. A. C. Leckey, "Characterization of impact damage in composite laminates using guided wavefield imaging and local wavenumber domain analysis," *Ultrasonics,* 53 (7), pp. 1217-1226, 2013.

[23] L. Yu and Z. Tian, "Lamb wave structural health monitoring using a hybrid pzt-laser vibrometer approach," *Structural Health Monitoring,* 12 pp. 469-483, 2013.

[24] M. S. Harb and F. G. Yuan, "A rapid, fully non-contact, hybrid system for generating lamb wave dispersion curves," *Ultrasonics,* 61 pp. 62-70, 2015.

[25] P. Kudela, M. Radzienski, and W. Ostachowicz, "Identification of cracks in thin-walled structures by means of wavenumber filtering," *Mechanical Systems and Signal Processing,* 50-51 pp. 456-466, 2015.

[26] E. B. Flynn, S. Y. Chong, G. J. Jarmer, and J. R. Lee, "Structural imaging through local wavenumber estimation of guided waves," *Ndt & E International,* 59 pp. 1-10, 2013.

[27] Z. Tian, L. Yu, C. Leckey, and J. Seebo, "Guided wave imaging for detection and evaluation of impact-induced delamination in composites," *Smart Materials and Structures,* 24 (10), p. 105019, 2015.

[28] O. Mesnil, C. A. C. Leckey, and M. Ruzzene, "Instantaneous and local wavenumber estimations for damage quantification in composites," *Structural Health Monitoring,* 14 pp. 193-204, 2014.

[29] W. Ostachowicz, M. Radzienski, and P. Kudela, "50th anniversary article: Comparison studies of full wavefield signal processing for crack detection," *Strain,* 50 pp. 275-291, 2014.

[30] P. D. Juarez and C. A. C. Leckey, "Multi-frequency local wavenumber analysis and ply correlation of delamination damage," *Ultrasonics,* 62 pp. 56-65, 2015.

[31] D. Girolamo, H. Y. Chuang, and F. G. Yuan, "Impact damage visualization in a honeycomb composite panel through laser inspection using zero-lag cross-correlation imaging condition," *Ultrasonics,* 87 pp. 152-165, 2018.

[32] J. S. Hall, P. Fromme, and J. E. Michaels, "Guided wave damage characterization via minimum variance imaging with a distributed array of ultrasonic sensors," *Journal of Nondestructive Evaluation,* 33 (3), pp. 299-308, 2014.

[33] L. Yu and C. Leckey, "Lamb wave-based quantitative crack detection using a focusing array algorithm," *Journal of Intelligent Material Systems and Structures,* 24 (9), pp. 1138-1152, 2013.

[34] Z. Tian, L. Yu, X. Sun, and B. Lin, "Damage localization with fiber bragg grating lamb wave sensing through adaptive phased array imaging," *Structural Health Monitoring,* 18 (1), pp. 334-344, 2019.

[35] G. J. S. Jarmer, E. B. Flynn, and M. D. Todd, "Multi-wave-mode, multi-frequency detectors for guided wave interrogation of plate structures," *Structural Health Monitoring-an International Journal,* 13 (2), pp. 120-130, 2014.

[36] Z. Tian and L. Yu, "Lamb wave frequency-wavenumber analysis and decomposition," *Journal of Intelligent Material Systems and Structures,* 25 (9), pp. 1107-1123, 2014.
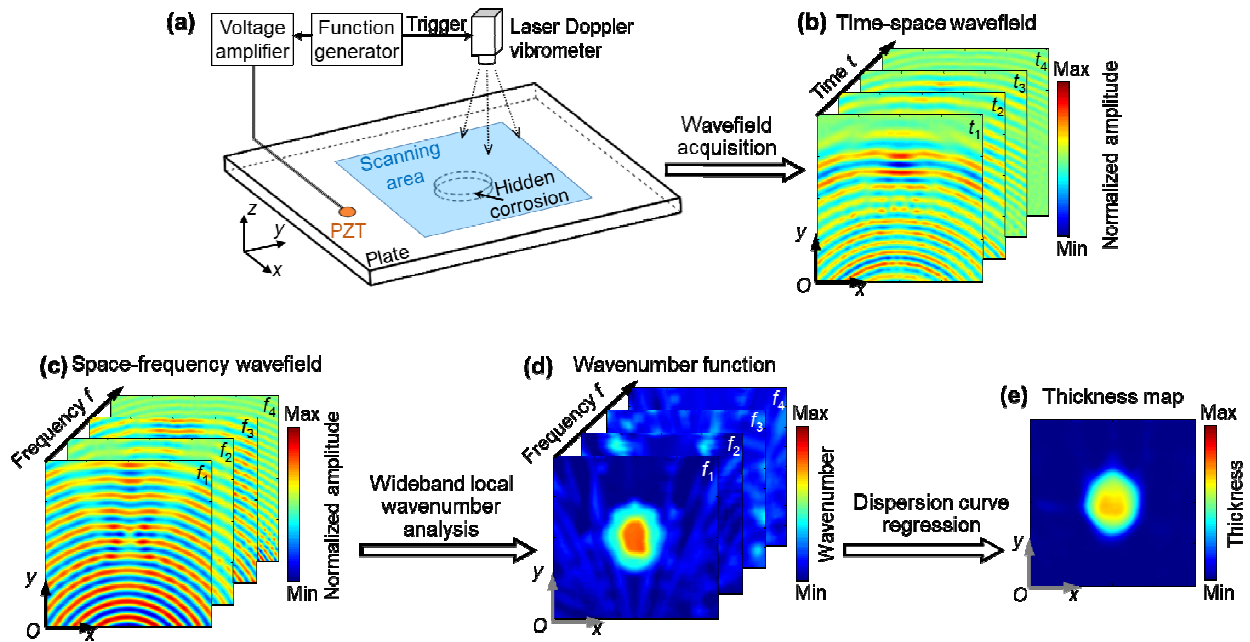
Figures

Figure 1.   Illustration of the dispersion curve regression-assisted wideband local wavenumber analysis for characterizing the 3D profile of hidden corrosion. (a) Sensing layout of a PZT-SLDV system for acquiring the time-space wavefield of Lamb waves. Figures from (b) to (e) show the procedures of our analysis method. The acquired time-space wavefield (b) is transformed to a space-frequency wavefield (c). Then, through wideband local wavenumber characterization, a local wavenumber function (d) is obtained. Through dispersion curve regression, we can further obtain a thickness map (e) for characterizing the 3D profile of hidden corrosion, i.e., the corrosion size and shape in the x and y dimensions and the corrosion depth in the z dimension.
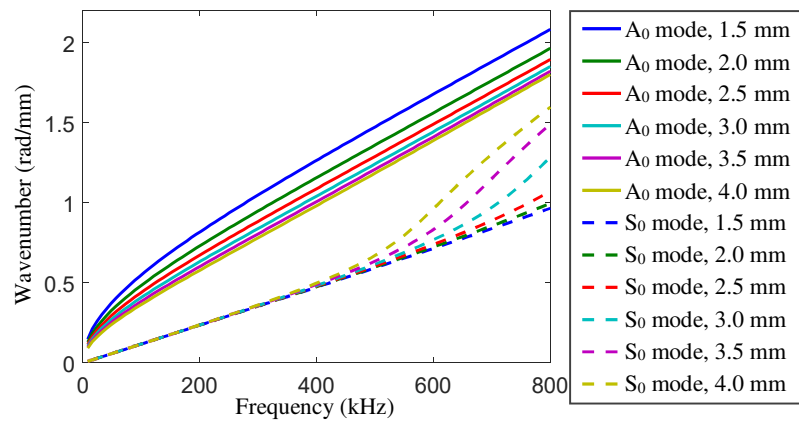
Figure 2.   Frequency-wavenumber dispersion curves of A_0 and S_0 modes in aluminum plates with different thicknesses from 1.5 to 4 mm. Compared to S_0 mode's wavenumber, the A_0 mode's wavenumber is more sensitive to the plate thickness in the range 0 – 600 kHz, while less sensitive in the range 600 – 800 kHz. The material properties used for calculating dispersion curves includes Poisson's ratio 0.33, Young's modulus 69 GPa, and density 2700 kg/m^3.
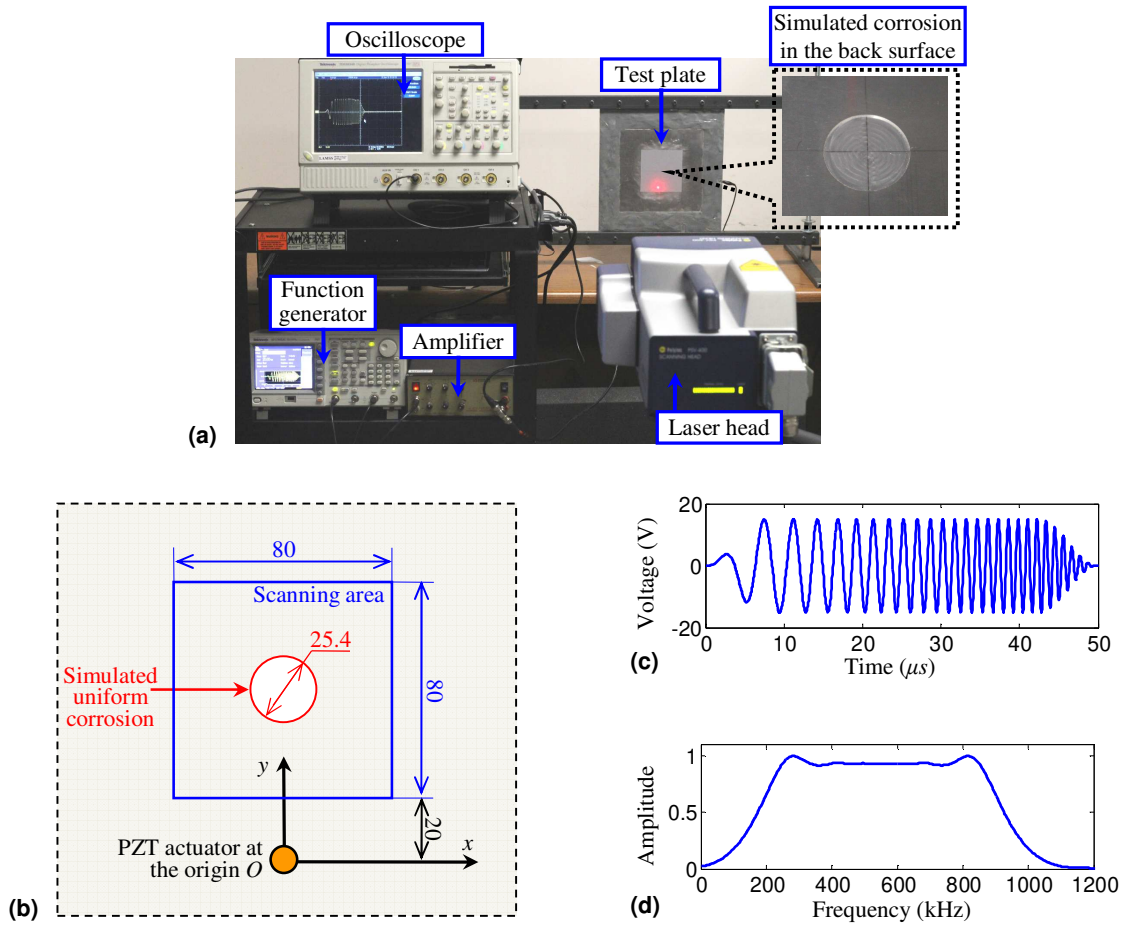
Figure 3.   Experimental setup for detecting hidden uniform corrosion in a 3.2 mm thick aluminum plate. (a) Photos of the experimental setup and the uniform corrosion. (b) A schematic of the sensing layout (unit: mm). (c) and (d) are the waveform and frequency spectrum of the used chirp excitation signal, respectively.
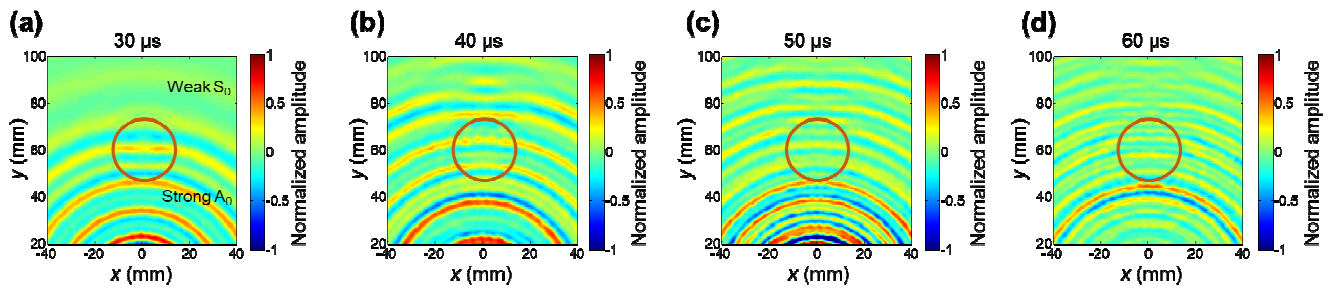
Figure 4.   Experimental wavefields acquired in an aluminum plate containing a circular-shaped uniform corrosion defect with a depth of 0.75 mm. (a-d) Acquired wavefields at 30, 40, 50, and 60 µs, respectively. It can be seen that the wavelengths gradually become smaller as time increases. The solid circle represents the actual area of the corrosion.
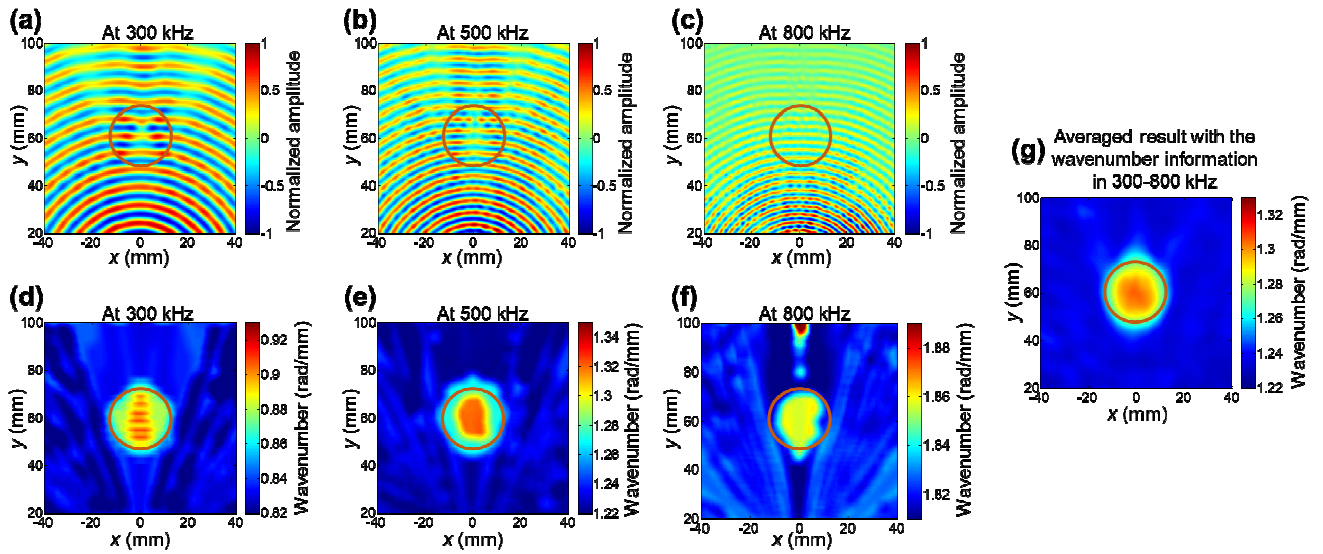
Figure 5. Results of wideband local wavenumber characterization for an aluminum plate containing a circular shaped uniform corrosion defect with a depth of 0.75 mm. (a-c) Wavefields at 300, 500, and 800 kHz obtained by applying Fourier transform to the experimentally acquired time-space wavefield. (d-f) Local wavenumber distributions at 300, 500, and 800 kHz obtained by applying local wavenumber analysis to the wavefields in (a-c). (g) The averaged local wavenumber distribution obtained by averaging a series of single-frequency local wavenumber distributions in the frequency range 300 – 800 kHz. Compared to single-frequency local wavenumber distributions in (d-f), the average local wavenumber distribution has lower noises and the detected damage area (high wavenumber region) agrees better with the actual area of the circular shaped corrosion.
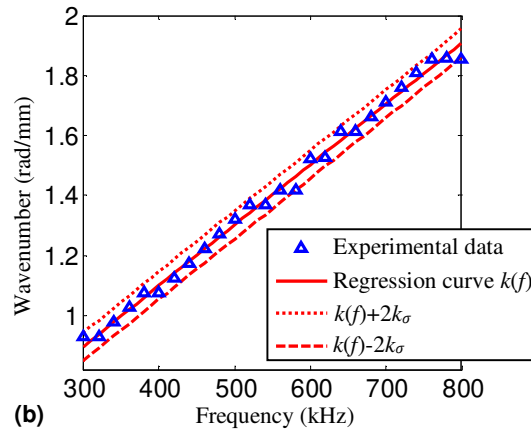
(b)

Figure 6.   Dispersion curve regression result at the location of (0, 60) mm, when the corrosion depth is 0.75 mm. The triangles are experimental data extracted from the local wavenumber function $k_{sw}(\bar{\mathbf{x}}, f)$. The solid line is the least square regression result, which is the dispersion curve that best matches the experimental data. The dotted and broken lines represent the upper and lower boundaries of the 95% confident region. The material properties used for calculating theoretical dispersion curves are Poisson's ratio 0.33, Young's modulus 69 GPa, and density 2700 kg/m^3.
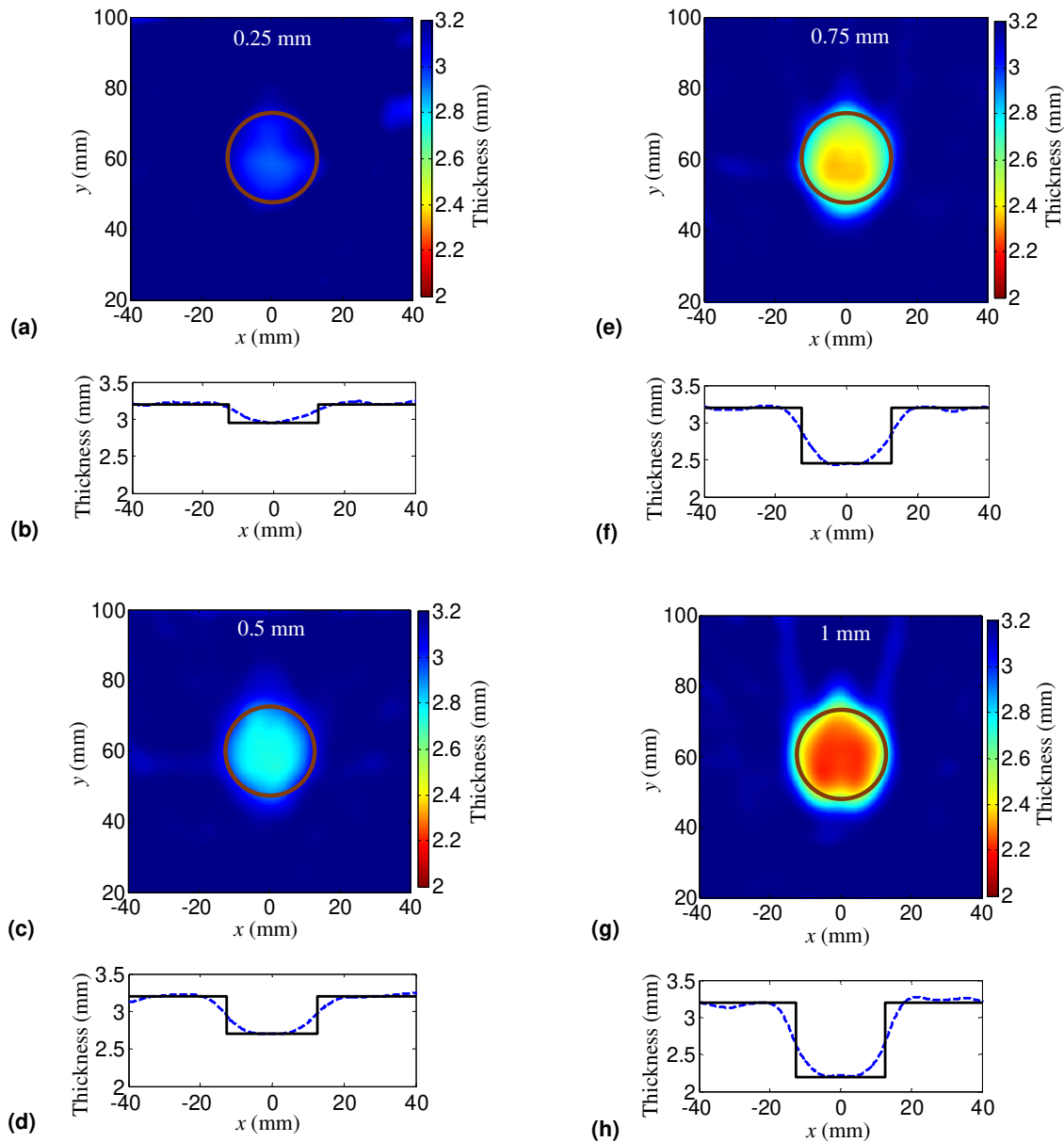
Figure 7.   Results of corrosion visualization and wall thickness quantification. (a), (c), (e) and (g) are thickness maps, when corrosion depths are 0.25, 0.50, 0.75, and 1.00 mm, respectively. The solid circle represents the actual area of corrosion for comparison purposes. (b), (d), (f) and (h) are thickness profiles along the line y = 60 mm, when corrosion depths are 0.25, 0.50, 0.75, and 1.00 mm, respectively. The solid and broken lines represent the actual thickness profile and the thickness mapping result, respectively.
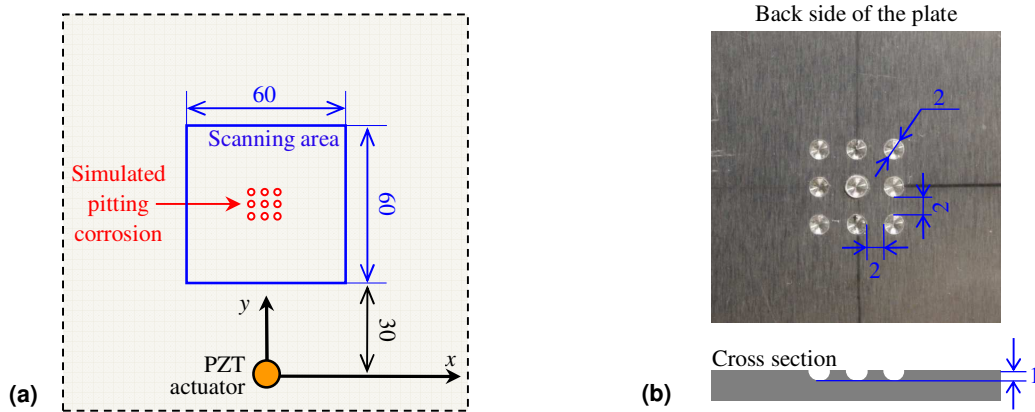
Figure 8.   Experimental layout for imaging simulated pitting corrosion in a 3.2 mm thick aluminum plate. (a) A schematic of the experimental layout. (b) A photo and a schematic of the pitting corrosion (unit: mm).
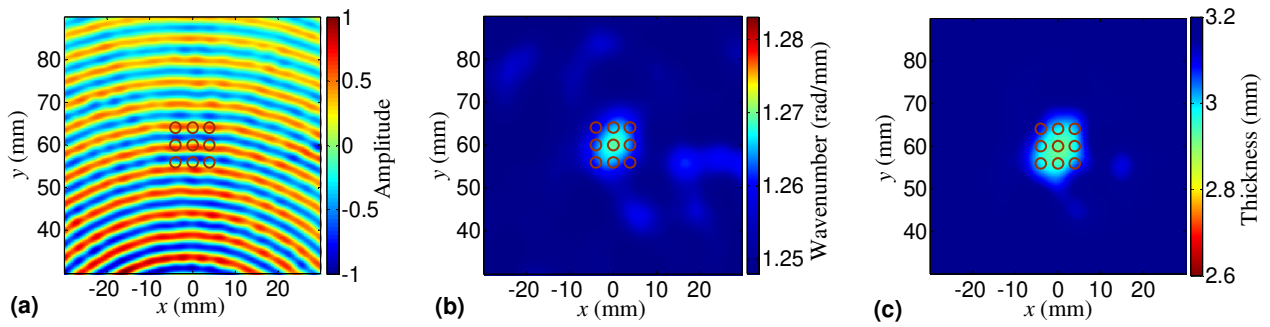
Figure 9. Wavefield analysis results for the plate with pitting corrosion. (a) The wavefield of A_0 mode at 500 kHz measured by the SLDV. (b) The averaged local wavenumber distribution in the frequency range 300 – 800 kHz. (c) The thickness mapping result. The 3×3 circles represent the 3×3 pits of the corrosion.